# Self-Assembled Plasmonic Nanoparticle Clusters

Jonathan A. Fan, *et al.*

*Science* **328**, 1135 (2010);
DOI: 10.1126/science.1187949

30. R. G. Scollay, E. C. Butcher, I. L. Weissman, *Eur. J. Immunol.* **10**, 210 (1980).
31. R. Pappu *et al.*, *Science* **316**, 295 (2007).
32. G. Bergers, S. Song, *Neuro-oncol.* **7**, 452 (2005).
33. M. Krueger, I. Bechmann, *Glia* **58**, 1 (2010).
34. K. Foster *et al.*, *J. Immunol.* **180**, 3183 (2008).
35. S. M. Müller *et al.*, *J. Immunol.* **180**, 5344 (2008).
36. Y. Chai *et al.*, *Development* **127**, 1671 (2000).
37. T. H. Pham *et al.*, *J. Exp. Med.* **207**, 17 (2010).
38. K. Venkataraman *et al.*, *Circ. Res.* **102**, 669 (2008).
39. M. Drumea-Mirancea *et al.*, *J. Cell Sci.* **119**, 1396 (2006).
40. R. C. Ji, K. Kurihara, S. Kato, *Anat. Sci. Int.* **81**, 201 (2006).
41. R. M. Bearman, K. G. Bensch, G. D. Levine, *Anat. Rec.* **183**, 485 (1975).
42. We thank J. Lingrel for making KLF2$^{f/f}$ mice available and K. Hogquist for sending these mice; S. Coughlin for Sphk1$^{f/-}$2$^{-/-}$ mice; T. Nakayama for CD69$^{-/-}$; B. Black for providing Wnt1-Cre mice; T. Pham, Y. Xu, and J. An for technical help; F. Schaufele of the Diabetes Endocrinology Research Center Imaging Core for help with the confocal microscope core; N. Killeen for help generating the S1P1 transgenic mice; and O. Bannard, S. Coughlin, M. Anderson, and A. Weiss for comments on the manuscript. M.A.Z. was supported by the UCSF Medical Scientist Training Program. J.G.C. is an investigator of the Howard Hughes Medical Institute. This work was supported in part by NIH grant AI74847.

**Supporting Online Material**

www.sciencemag.org/cgi/content/full/science.1188222/DC1
Materials and Methods
Figs. S1 to S5
Movies S1 and S2
References

11 February 2010; accepted 9 April 2010
Published online 22 April 2010;
10.1126/science.1188222
Include this information when citing this paper.

REPORTS

# Self-Assembled Plasmonic Nanoparticle Clusters

**Jonathan A. Fan,[1] Chihhui Wu,[2] Kui Bao,[3] Jiming Bao,[4] Rizia Bardhan,[5] Naomi J. Halas,[5] Vinothan N. Manoharan,[1,6] Peter Nordlander,[3] Gennady Shvets,[2] Federico Capasso[1]***

The self-assembly of colloids is an alternative to top-down processing that enables the fabrication of nanostructures. We show that self-assembled clusters of metal-dielectric spheres are the basis for nanophotonic structures. By tailoring the number and position of spheres in close-packed clusters, plasmon modes exhibiting strong magnetic and Fano-like resonances emerge. The use of identical spheres simplifies cluster assembly and facilitates the fabrication of highly symmetric structures. Dielectric spacers are used to tailor the interparticle spacing in these clusters to be approximately 2 nanometers. These types of chemically synthesized nanoparticle clusters can be generalized to other two- and three-dimensional structures and can serve as building blocks for new metamaterials.

Subwavelength metallic structures enable the broad manipulation of electromagnetic fields at the nanoscale (*1*, *2*) because of their ability to support surface plasmons, which are oscillations of free electrons in metal that couple with the electromagnetic field. The optical properties of these structures depend sensitively on their geometry, making it possible to engineer their electric and magnetic responses over a broad range. Ensembles of nanostructures can be used to construct metamaterials in which the refractive index can be tailored from positive to negative (*2*–*4*) and the polarization of an incident field can be filtered (*5*) or rotated. Individual nanostructures can function as nanoscale laser cavities (*6*) and elements in optical nanocircuits (*7*), and their coupling can support nanoscale light transport (*8*). The strong field localization that arises in these structures at their resonances has applications in sensing (*9*), surface-enhanced spectroscopies, and nonlinear optics (*5*, *10*).

Traditionally, plasmonic nanostructures are fabricated on planar substrates by top-down processes such as electron-beam lithography or focused–ion beam milling. With these methods, geometries as varied as split rings and coupled nanorods can be patterned with precise substrate positioning, leading to structures that support electric, magnetic (*3*, *11*), and Fano-like resonances (*12*, *13*). Fano-like resonances arise from interactions between a superradiant "bright" mode and a subradiant "dark" mode in a nanostructure, and they are characterized by a pronounced minimum in the scattering spectra. These fabrication routes have several fundamental limitations. First, the spatial resolution of the structures is limited to ~10 nm by the electron- and ion-beam size and the metal grain size. Second, these routes produce planar thin-film architectures that are generally unsuitable for complex three-dimensional (3D) fabrication. Third, there is limited optical coupling between thin-film nanostructures defined within the same plane. Stronger coupling can be attained by vertically stacking plasmonic structures (*3*, *13*), but this fabrication strategy is challenging.

The self-assembly of metallic colloids (*14*–*17*) provides a versatile and low-cost route to the construction of complex 2D and 3D optical materials. We show that self-assembled clusters of spherical metal-dielectric colloids have optical properties that can be controlled by varying the number and position of particles in the cluster. As such, a hierarchy of tunable plasmonic structures that exhibit strong electric, magnetic, and Fano-like resonances (Fig. 1A) is formed. The resonances in these structures arise from the strong electromagnetic coupling between closely spaced particles and can be described by plasmon hybridization (*18*). Clusters are assembled in a relatively straightforward manner with a capillary-driven method, and their interparticle spacing is controlled by polymer spacers to be ~2 nm, surpassing the spatial resolution of conventional lithography.

The assembly of colloidal clusters, shown schematically in Fig. 1B, starts with the synthesis of gold nanoshells, which consist of a silica core and metallic shell (*19*). Nanoshells are versatile structures in nanophotonics because their electric dipole resonances can be tuned from visible to mid-infrared wavelengths by varying their core-shell aspect ratios. Their spherical geometry, derived from their smooth and spherical silica cores, supports orientation-independent optical coupling, which greatly simplifies their controlled assembly. This isotropy also enables the construction of highly symmetric clusters. Next, the nanoshells are coated with a polymer in the form of a self-assembled monolayer (*20*), which defines the gap separation between nanoparticles in the clusters and sets the magnitude of interparticle electromagnetic coupling. Clusters are assembled by slowly drying a droplet of the particles on a hydrophobic substrate at room temperature. The optical properties of individual clusters are measured by dark-field spectroscopy (Fig. 1C) (*21*). To better distinguish higher-order modes that would otherwise be obscured by broad electric dipole scattering, a cross-polarizer is used in measurements with *s*-polarized incident light to filter out scattered electric dipole radiation (*22*). Details regarding sample preparation and the measurement scheme are available in the supporting online material (SOM).

The trimer, consisting of three nanoshells of equilateral spacing, is among the simplest cluster geometries to display interesting resonances; it supports a magnetic dipole mode. The modes of this structure can be understood from a rigorous analysis in the quasistatic limit (i.e., the structure is scaled to be much smaller than the wavelength

[1]School of Engineering and Applied Sciences, Harvard University, 29 Oxford Street, Cambridge, MA 02138, USA. [2]Department of Physics, University of Texas at Austin, 1 University Station C1600, Austin, TX 78712, USA. [3]Department of Physics, Rice University, MS 61, Houston, TX 77005, USA. [4]Department of Electrical and Computer Engineering, University of Houston, 4800 Calhoun Road, Houston, TX 77204, USA. [5]Department of Electrical and Computer Engineering, Rice University, 6100 Main Street, MS-366, Houston, TX 77005, USA. [6]Department of Physics, Harvard University, 17 Oxford Street, Cambridge, MA 02138, USA.

*To whom correspondence should be addressed. E-mail: capasso@seas.harvard.edu

of incident light), which reveals their symmetries and resonant frequencies. This analysis also provides a guide to interpreting the spectra of finite-sized trimers, which have resonances that are qualitatively similar but red-shifted relative to the quasistatic ones (*23*). The resonant wavelengths for different trimer modes as a function of gap separation (Fig. 2A) show all of the modes red-shifting with decreasing gap separation due to enhanced capacitive coupling between the nanoshells. The two electric dipole modes are degenerate in energy and correspond to two different orientations relative to the trimer; this degeneracy is explained by the $D_{3h}$ point group characterizing the cluster, which supports isotropic in-plane resonances (*24*). A plot of the electric potential and displacement fields for a magnetic mode is shown in the inset of Fig. 2A. A circulating field, which is a hallmark of the magnetic moment, is clearly visible. The particularly strong capacitive interaction at the nanoshell gaps red-shifts this mode well past all of the other modes.

The scattering spectra and transmission electron microscopy (TEM) image of an individual trimer consisting of three 40-nm-thick gold nanoshells are shown in Fig. 2B. Thicker shells are synthesized to increase the total polarizability of the structure. The trimer is probed by incident *s*- and *p*-polarization, which correspond to the electric field oriented in and out of the trimer plane, respectively. A gap separation of 2.5 nm provides a good match between the experimental and calculated electric dipole peak positions. A comparison between the experimental and theoretical spectra shows good agreement. In both cases, the *s*-polarized spectra have an electric dipole peak near 1200 nm and higher-order modes at 600 to 700 nm. Any magnetic dipole peak is obscured by the broad electric dipole. The *p*-polarized spectra in both cases have a sharp peak near 700 nm, which represent out-of-plane plasmon resonances. The oscillations in the *p*-polarized experimental spectrum are artifacts caused by interference from light scattered by the rough metallic TEM grid in the trimer vicinity.

Evidence for a magnetic dipole mode comes from spectra taken with the cross-polarizer in the light path (Fig. 2C), which suppresses the maximum peak intensity in the measured spectrum by a factor of 11. Electric dipole radiation is filtered less effectively here by the polarizer, compared with that from a single nanoshell (fig. S2), due to optical activity in the trimer [see (*25*) and the SOM]. In both the calculated and experimental spectra, a narrow peak near 1400 nm becomes visible. There is strong evidence that this feature is the magnetic dipole peak. First, a direct calculation of the magnetic dipole moment perpendicular to the trimer (presented in the inset of Fig. 2C) shows a sharply peaked magnetic dipole near 1400 nm. Second, the linewidths of the experimental feature and the theoretical magnetic dipole are distinctly narrow and match. Finally, the peak is substantially red-shifted relative to the electric

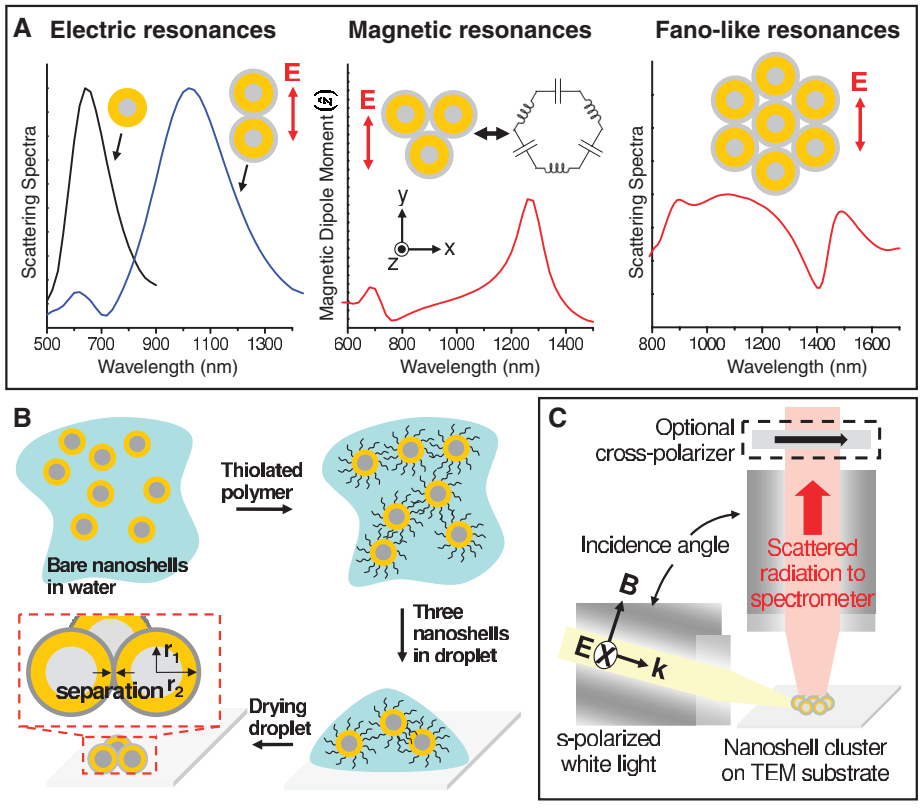


**Fig. 1.** Self-assembled nanoshell clusters as nanoplasmonic components. (**A**) Nanoshell clusters can be tailored to support tunable electric, magnetic, and Fano-like resonances. Electric dipole resonances generally exist for all plasmonic nanostructures and are shown here for individual nanoshells and coupled dimers. Packed trimer clusters exhibit magnetic dipole resonances and can be described as a closed loop of nanoinductors and nanocapacitors. Fano-like resonances are supported by heptamers. These simulations use nanoshells with $[r_1, r_2] = [62.5, 85]$ nm (where $r_1$ and $r_2$ are the inner and outer radii of the gold shell, respectively), and the clusters have 2-nm-wide gaps filled with a dielectric spacer with a dielectric constant $\varepsilon = 2.5$. E, electric field. (**B**) To assemble the clusters, nanoshells in aqueous solution are coated with a polymer. A dilute droplet of particles is then placed on a hydrophobic substrate and evaporated. During this process, the droplet breaks into smaller droplets, and nanoshells within these smaller droplets pack together by capillary forces. The nanoshell geometry and polymer-spacer separation are defined. (**C**) To measure scattering spectra, white light is polarized and focused onto the sample, and scattered light from an individual cluster is collected and analyzed in a spectrometer. The optional cross-polarizer is oriented 90° relative to the incident-light polarization. B, magnetic field; k, wave vector of incident light.

dipole, which is consistent with the quasistatic theory (Fig. 2A). The differences between the experimental and calculated cross-polarized spectra at wavelengths shorter than 1100 nm are probably due to small geometric anisotropies in the synthesized trimer (*26*) and to the complex interaction between the trimer and thin-film substrate (see fig. S3).

Heptamers, which are symmetric clusters composed of seven equivalent elements, support complex plasmon mode interactions that lead to Fano-like interference. Fano-like interference involves a continuum of incident photons (I), a superradiant bright mode (B) that couples to (I), and a subradiant dark mode (D) that does not couple to (I) but instead couples to the bright mode via a near-field interaction. At frequencies resonant with both the bright and dark modes, the former will be excited via two pathways: (i) $|I\rangle \rightarrow |B\rangle$ and (ii) $|I\rangle \rightarrow |B\rangle \rightarrow |D\rangle \rightarrow |B\rangle$. At the Fano minimum, these two pathways destructively interfere and cancel the polarization of the bright mode. The result is a narrow minimum in the scattering and extinction spectra.

These mode interactions are absent in simpler clusters such as the dimer and trimer, which are characterized by a superradiant electric dipole resonance in their scattering spectra (Figs. 1A and 2B) but support no visible Fano minima. Additional structural complexity is required for the clusters to support interacting bright and dark modes. One approach is to break the symmetry of the dimer or trimer, which would lead to the formation of new dark modes. With the heptamer here, the strong electromagnetic coupling between seven particles creates new plasmon modes that support Fano-like resonances, without the expense of symmetry breaking. Coupling between the bright and dark modes can be explained by group theory, as both modes share

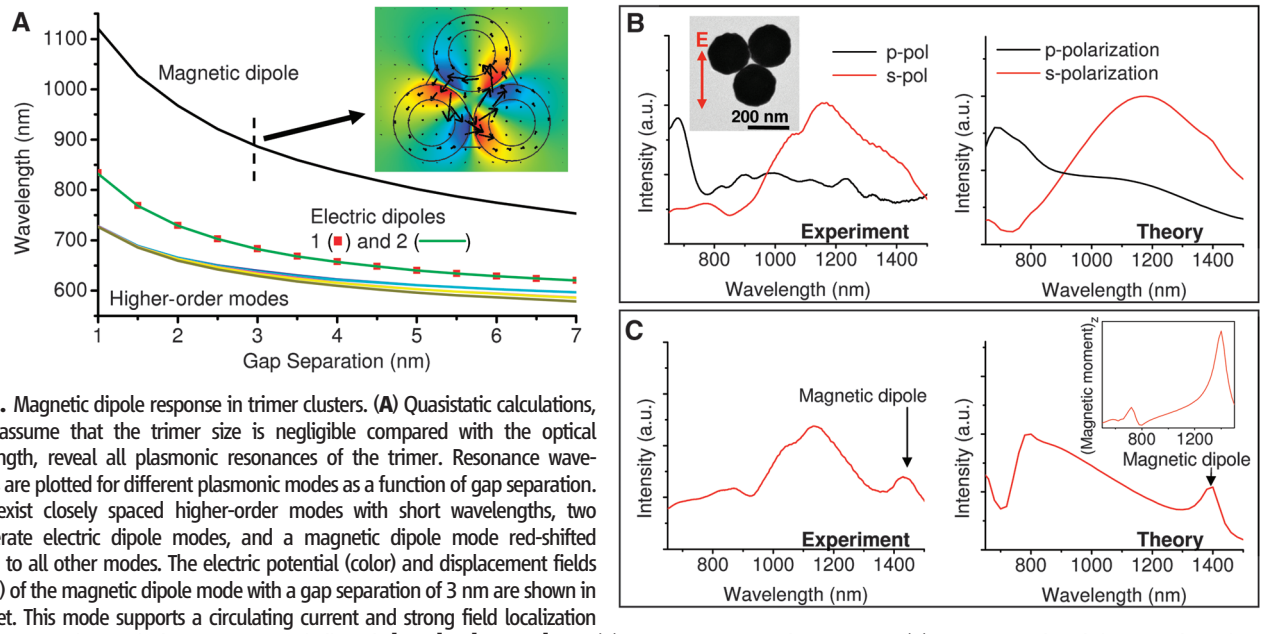


**Fig. 2.** Magnetic dipole response in trimer clusters. (**A**) Quasistatic calculations, which assume that the trimer size is negligible compared with the optical wavelength, reveal all plasmonic resonances of the trimer. Resonance wavelengths are plotted for different plasmonic modes as a function of gap separation. There exist closely spaced higher-order modes with short wavelengths, two degenerate electric dipole modes, and a magnetic dipole mode red-shifted relative to all other modes. The electric potential (color) and displacement fields (arrows) of the magnetic dipole mode with a gap separation of 3 nm are shown in the inset. This mode supports a circulating current and strong field localization near the gaps. These calculations use nanoshells with $[r_1, r_2]$ = [62, 102] nm. (**B**) Experimental and theoretical *s*- and *p*-polarized scattering spectra for an individual trimer shown in the inset. These spectra are dominated by the scattered electric dipole radiation from the cluster. The incidence angle of the white-light source is 78°, and its polarization orientation relative to the trimer is shown in the inset. The simulations use nanoshells with $[r_1, r_2]$ = [62, 102] nm and gap separations of 2.5 nm. a.u., arbitrary units. (**C**) Experimental and theoretical *s*-polarized scattering spectra for the same trimer and orientation in (B), but with insertion of the cross-polarizer. Both spectra now exhibit a clearly visible magnetic dipole peak, matching in peak position and linewidth. The inset shows the calculated magnitude of the trimer magnetic dipole moment in the *z* direction (see Fig. 1A for axis), confirming the nature of the spectral peak near 1400 nm.

symmetries from the same irreducible representation (*27*).

The Fano-like resonance is displayed in the calculated extinction spectrum of a heptamer (Fig. 3A). The interfering bright and dark modes of the cluster can be characterized by surface charge density plots at their resonances. The charge density plot of the bright mode at its peak at 1160 nm shows the charge oscillations in each nanoshell oriented in the same direction, resulting in strong scattering due to the constructive interference of their radiated fields. The charge density plot at the dark-mode peak frequency at 1490 nm shows only the dark mode, indicating that the bright mode is suppressed and that energy is stored in the dark mode. Here, the charge oscillations in the individual nanoshells are oriented in different directions, resulting in the destructive interference of their radiated fields. Calculations in the quasistatic limit (*27*) show that the dipole moment of the outer hexagon is similar in magnitude but opposite in sign to the dipole moment of the central particle, leading to strong destructive interference of their radiating fields.

We observe a strong Fano-like resonance in the experimental spectra. The TEM image of a single heptamer and its spectra for three different orientations are shown in Fig. 3B. The scattering spectrum at each orientation shows a strong Fano minimum at 1450 nm. This isotropy is consistent with the symmetry of the heptamer ($D_{6h}$ point group), which supports isotropic, in-plane resonances (*27*). The peaks between 800 and 1300 nm are higher-order modes that arise from retardation effects created by the large in-

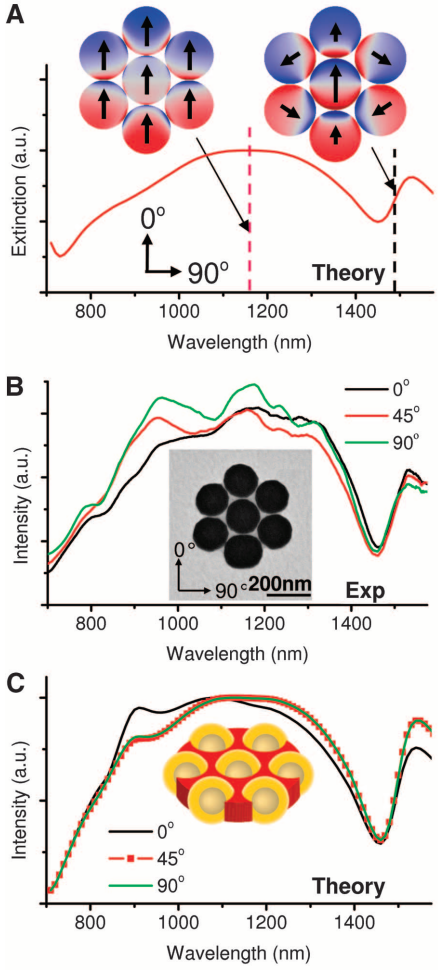


**Fig. 3.** Fano-resonant behavior of a plasmonic heptamer. (**A**) Calculated extinction spectrum and charge density plots for a heptamer excited at normal incidence with a 0° orientation angle. The nanoshells have dimensions $[r_1, r_2]$ = [62.5, 85] nm, and the cluster has 1.6-nm gap separations and is embedded in a cylinder with a dielectric constant $\varepsilon$ = 2.5. The Fano minimum, characterized by suppression of the bright mode, is at 1450 nm. The charge density plot of the bright mode, whose peak resonance is denoted by the pink dashed line at 1160 nm, shows the charge oscillations on each nanoshell oriented in the same direction, resulting in the constructive interference of their radiated fields. The charge density plot of the heptamer at 1490 nm, denoted by the black dashed line, shows the dark mode at its peak resonance. This mode supports charge oscillations on the nanoshells oriented in different directions, resulting in the destructive interference of their radiated fields. (**B**) TEM image and spectra of a heptamer at three different incident electric-field orientation angles. The nanoshells are measured to have average dimensions $[r_1, r_2]$ = [62.5, 85] nm. The Fano minimum at 1450 nm is isotropic for these orientation angles. (**C**) Calculated scattering spectra for a heptamer with a geometry matching that in (A), for the three orientation angles in (B).

cidence angle. The calculated scattering spectra of a heptamer for different polarization angles are shown in Fig. 3C, where the cluster geometry is identical to that used in Fig. 3A. These spectra display Fano minima at 1450 nm, with asymmetric line shapes that match the experimental spectra. The nanoshell separation modeled here is smaller than that used for the trimer calculations to account for the strongly red-shifted Fano minimum. This red shift is probably due to a combination of at least three factors: (i) smaller nanoshell separation due to inhomogeneous self-assembled monolayer coverage, (ii) a higher–refractive-index environment near the cluster due to excess polymer deposition, and (iii) increased capacitive coupling between the nanoparticles due to nanoshell faceting.

This cluster concept can be generalized to other functional 2D and 3D structures. One example is the tetrahedral cluster, which supports isotropic electric and magnetic resonances in three dimensions (*28*) and can be used as a building block for isotropic metamaterials. Symmetry breaking can be applied to engineer other types of optical modes: Trimers comprising three different particle types support magnetoelectric modes, and tetrahedral clusters comprising four different particle types are chiral. Nonspherical plasmonic particles can be used to construct more elaborate structures, provided that their orientations can be controlled during assembly. In all of these structures, resonances can be tuned by varying individual particle geometries, interparticle separation, and the dielectric environment of the cluster. The assembly of clusters from solution is highly versatile: It can lead to liquid metamaterials or "metafluids" (*28*), be integrated into soft materials such as gels, or be encapsulated and dried onto surfaces of arbitrary curvature or patterning. Future work will focus on these applications and on achieving higher cluster yields comparable to those attained with lithographically defined patterns (*29*), emulsion droplets (*30*), and DNA linking (*31*).

### References and Notes


1. W. L. Barnes, A. Dereux, T. W. Ebbesen, *Nature* **424**, 824 (2003).
2. V. M. Shalaev, *Nat. Photonics* **1**, 41 (2007).
3. V. M. Shalaev *et al.*, *Opt. Lett.* **30**, 3356 (2005).
4. J. B. Pendry, D. Schurig, D. R. Smith, *Science* **312**, 1780 (2006); published online 25 May 2006 (10.1126/science.1125907).
5. M. W. Klein, C. Enkrich, M. Wegener, S. Linden, *Science* **313**, 502 (2006).
6. D. J. Bergman, M. I. Stockman, *Phys. Rev. Lett.* **90**, 027402 (2003).
7. N. Engheta, *Science* **317**, 1698 (2007).
8. S. A. Maier *et al.*, *Adv. Mater.* **13**, 1501 (2001).
9. L. J. Sherry *et al.*, *Nano Lett.* **5**, 2034 (2005).
10. J. B. Pendry, A. J. Holden, D. J. Robbins, W. J. Stewart, *IEEE Trans. Microwave Theory Tech.* **47**, 2075 (1999).
11. T. J. Yen *et al.*, *Science* **303**, 1494 (2004).
12. N. Verellen *et al.*, *Nano Lett.* **9**, 1663 (2009).
13. N. Liu *et al.*, *Nat. Mater.* **8**, 758 (2009).
14. K. J. Stebe, E. Lewandowski, M. Ghosh, *Science* **325**, 159 (2009).
15. T. Ming *et al.*, *Angew. Chem. Int. Ed.* **47**, 9685 (2008).
16. J. H. Lee, Q. Wu, W. Park, *Opt. Lett.* **34**, 443 (2009).
17. M. S. Wheeler, J. S. Aitchison, J. I. L. Chen, G. A. Ozin, M. Mojahedi, *Phys. Rev. B* **79**, 073103 (2009).
18. E. Prodan, C. Radloff, N. J. Halas, P. Nordlander, *Science* **302**, 419 (2003).
19. S. J. Oldenburg, R. D. Averitt, S. L. Westcott, N. J. Halas, *Chem. Phys. Lett.* **288**, 243 (1998).
20. J. C. Love, L. A. Estroff, J. K. Kriebel, R. G. Nuzzo, G. M. Whitesides, *Chem. Rev.* **105**, 1103 (2005).
21. J. J. Mock, M. Barbic, D. R. Smith, D. A. Schultz, S. Schultz, *J. Chem. Phys.* **116**, 6755 (2002).
22. C. Enkrich *et al.*, *Phys. Rev. Lett.* **95**, 203901 (2005).
23. Y. A. Urzhumov, G. Shvets, *Solid State Commun.* **146**, 208 (2008).
24. D. W. Brandl, N. A. Mirin, P. Nordlander, *J. Phys. Chem. B* **110**, 12302 (2006).
25. E. Plum *et al.*, *Phys. Rev. Lett.* **102**, 113902 (2009).
26. Random symmetry breaking can be experimentally addressed by using smoother thick-shelled nanoparticles, assembling nanoparticles with atomically smooth facets such as crystalline nanocubes, or assembling clusters with larger gap sizes, which would effectively reduce gap geometry variation (but at the expense of total mode strength).
27. N. A. Mirin, K. Bao, P. Nordlander, *J. Phys. Chem. A* **113**, 4028 (2009).
28. Y. A. Urzhumov *et al.*, *Opt. Express* **15**, 14129 (2007).
29. Y. D. Yin, Y. Lu, B. Gates, Y. N. Xia, *J. Am. Chem. Soc.* **123**, 8718 (2001).
30. V. N. Manoharan, M. T. Elsesser, D. J. Pine, *Science* **301**, 483 (2003).
31. C. J. Loweth, W. B. Caldwell, X. G. Peng, A. P. Alivisatos, P. G. Schultz, *Angew. Chem. Int. Ed.* **38**, 1808 (1999).



32. J.A.F., F.C., C.W., and G.S. acknowledge funding by the NSF Nanoscale Interdisciplinary Research Team under grant no. ECCS-0709323; G.S. and C.W. acknowledge funding by Air Force Office of Scientific Research (AFOSR) Multidisciplinary University Research Initiative grants FA9550-06-1-0279 and FA9550-08-1-0394; R.B, N.J.H., and P.N. acknowledge support from the U.S. Department of Defense National Security Science and Engineering Faculty Fellowship program, the Robert A. Welch Foundation (C-1220 and C-1222), AFOSR grant F49620-03-C-0068, the SUG@R (Shared University Grid at Rice) team, and the Center for Advanced Solar Photophysics, a U.S. Department of Energy Energy Frontier Research Center. Electron microscopy was performed at the Center for Nanoscale Science at Harvard University, a member of the National Nanotechnology Infrastructure Network. J.A.F. acknowledges R. Guerra for helpful discussions and D. Bell for EM support.


### Supporting Online Material

www.sciencemag.org/cgi/content/full/328/5982/1135/DC1
Materials and Methods
SOM Text
Figs. S1 to S6
References

4 February 2010; accepted 22 April 2010
10.1126/science.1187949

# How Grain Growth Stops: A Mechanism for Grain-Growth Stagnation in Pure Materials

**Elizabeth A. Holm* and Stephen M. Foiles**

**The thermodynamic equilibrium state of crystalline materials is a single crystal; however, polycrystalline grain growth almost always stops before this state is reached. Although typically attributed to solute drag, grain-growth stagnation occurs, even in high-purity materials. Recent studies indicate that grain boundaries undergo thermal roughening associated with an abrupt mobility change, so that at typical annealing temperatures, polycrystals will contain both smooth (slow) and rough (fast) boundaries. Mesoscale grain-growth models, validated by large-scale polycrystalline molecular dynamics simulations, show that even small fractions of smooth, slow boundaries can stop grain growth. We conclude that grain-boundary roughening provides an alternate stagnation mechanism that applies even to high-purity materials.**

Most metals and ceramics are polycrystalline: They are made up of many individual crystallites, called grains, separated by internal interfaces or grain boundaries. When polycrystalline materials are annealed at sufficiently high temperatures, grain boundaries move and rearrange so as to increase the average grain size and decrease the grain-boundary area per unit volume. However, even at very high temperatures, grain growth only rarely proceeds to the equilibrium single-crystal state. Instead, grain growth usually stops, though substantial internal interface remains. In fact, grain stagnation is so pervasive that most grain-growth models presume a finite maximum grain size based purely on empirical observations (*1*).

Understanding and controlling grain growth is important to nearly every engineered material. For materials that rely on strength, toughness or formability, including most nanocrystalline materials, a stable, fine grain size is desirable. However, there are also important systems, such as superalloy turbine blades and silicon photovoltaics, in which a large (or even single-crystal) grain size is preferred.

There have been many grain-growth stagnation mechanisms proposed, each valid in certain regimes. Well-known processes that reduce the driving force for grain growth sufficiently to

Computational Materials Science and Engineering Department, Sandia National Laboratories, Albuquerque, NM 87185–1411, USA.

*To whom correspondence should be addressed. E-mail: eaholm@sandia.gov